CRACK PROPAGATION MODELING BY REMESHING USING THE CELL METHOD (CM)

Elena **Ferretti**

Nota Tecnica N° 55
Bologna – 2001

UNIVERSITÀ DEGLI STUDI DI BOLOGNA – FACOLTÀ DI INGEGNERIA
D.I.S.T.A.R.T. – DIPARTIMENTO DI INGEGNERIA DELLE STRUTTURE,
DEI TRASPORTI, DELLE ACQUE, DEL RILEVAMENTO E DEL TERRITORIO

V.le Risorgimento, 2 – 40136 Bologna

Crack propagation modeling by remeshing using the Cell Method (CM)

E. Ferretti[1]

Abstract: A numerical code for modeling crack propagation using the cell method is proposed. The Mohr-Coulomb criterion is used to compute the direction of crack propagation, and the new crack geometry is realized by an intra-element propagation technique. Automatic remeshing is then activated. Applications in Mode I and Mixed Mode are presented to illustrate the robustness of the implementation.

Keywords: Cell Method, fracture mechanics, crack propagation, automatic remeshing.

1 Introduction

Modeling the propagation of a crack through a mesh is difficult, since the geometry of the mesh must be modified as the crack propagates. Two different strategies are available to study fracture mechanics (FM) using the finite element method (FEM). The first strategy describes fracture as a sharp drop in the normal stress, due to the evolution of damage to the material [Gurson (1977), Rousselier (1981)]. The second strategy represents the crack as a displacement discontinuity described by the separation of its edges. Since this approach requires a remeshing stage to model the crack propagation, many authors have developed innovative techniques to simulate the propagation through a FEM mesh, such as the meshless method [Atluri and Shen (2002), Atluri and Zhu (1998), Kim and Atluri (2000), Nikishkov Park and Atluri (2001)], the element-free Galerkin method [Belytschko, Lu and Gu (1994)], the arbitrary local mesh replacement method [Rashid (1998)], the boundary element method, and nodal relaxation. In particular, nodal relaxation can be achieved using two different techniques: inter-element propagation, which is mesh dependent, since the crack propagates along mesh boundaries; and intra-element propagation, which is mesh independent, since the direction of propagation is computed using various criteria. The first method is faster than the second, since it does not require a remeshing stage, but it is less accurate.

Here, the second strategy has been chosen. A combination of nodal relaxation with intra-element propagation and remeshing has been adopted. This technique is used to implement a code using the cell method (CM) [Tonti (2001)].

The aim of this paper is not to present the most relevant fracture criteria or to discuss FM aspects, but to show how a CM numerical code can admit good predictions in FM. Consequently, a relatively simple fracture criterion is used: the Mohr-Coulomb criterion. For the same reason, only linear interpolation of the CM is used, and not quadratic interpolation [Cosmi (2000)].

Changes in mesh topology are rarely supported by classical FEM numerical codes. An example of a remeshing technique can be found in Bouchard, Bay, Chastel and Tovena (2000). The ability of a code to reproduce the change in mesh topology is of prime importance in FM. Thus, the present work is original in two ways. It is one of the first implementations of the CM for FM, and presents a remeshing technique that is easily able to take a general change in the mesh topology into account.

2 Theoretical basics of the CM

The CM is a new numerical method for solving field equations [Tonti (2001)]. The essence of this method is to provide a direct finite formulation of field equations, without requiring a differential formulation (Fig. 1).

All existing numerical methods for the solution of field equations take a differential formulation as their starting point. A finite formulation is derived from the differential formulation by one of various discretization methods (Fig. 1). Even the boundary element method (BEM) and the finite volume method (FVM), which use integral formulation, are based on a differential formulation. The CM is very similar to the direct or

[1] DISTART, University of Bologna, ITALY.

physical approach initially used in the FEM [Huebner (1975), Livesley (1983) and Fenner (1996)]. It is also similar to the FVM and can be considered as a generalization of the finite differences method (FDM). However, it was not possible to attain convergence greater than second order for any of these methods. Consequently, the physical approach fell out of favor. The CM (based on a different philosophy) permits the use of interpolation functions, as used in the FEM. This allows the physical approach to be revived. A demonstration of fourth-order convergence with the CM can be found in Cosmi (2000).

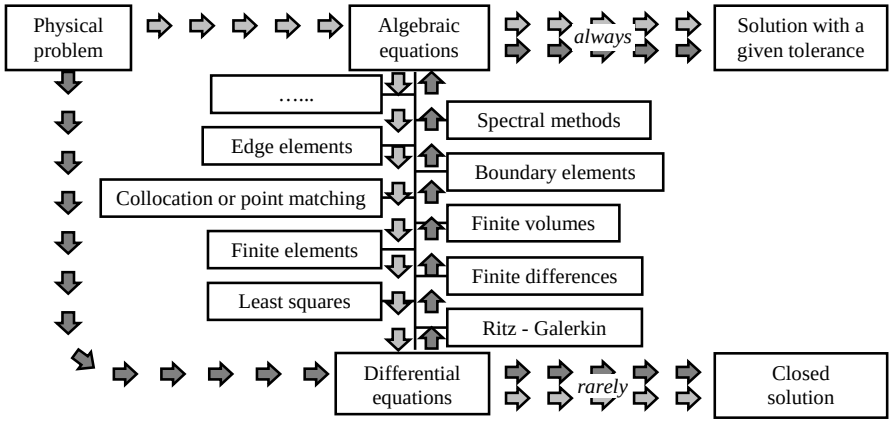

Figure 1: Comparison between the CM (⇨) and differential methods (➡)

The differential formulation requires field functions, which have to depend on point position and instant. Only on this condition is it possible to find the derivatives and, then, to apply the differential formulation. So, if the field functions are not directly described in terms of the current point and instant, they are obtained from global quantities, by performing densities and rates. The intention is to formulate the field laws in an exact form. However, the differential formulation can only be solved for very simple geometries and particular boundary conditions. To obtain a solution in the general case, the differential equations must be expressed in a discrete form (for any differential method). Consequently, the final solution is an approximation in all cases. It therefore seems unnecessary to use exact equations if, to solve them, we must introduce some kind of approximation.

The process of forming the densities of global quantities can be divided into two steps:

- dividing the global variable by the extent of the geometrical object to which it is referred, to obtain mean densities;
- performing the limit process of the mean densities with the extent of the geometrical object going to zero, to obtain point densities, that is, the required point functions.

The density finding process is usually carried out without considering whether there is a physical significance for the limit one is performing. In fact, since at the molecular scale matter is discrete, the notion of point density loses its physical sense.

Leaving the differential formulation, it is not more necessary to utilize point functions. This corresponds to replacing the idea of an exact solution with the idea of a solution within a given tolerance. Moving in this direction, the CM deals with (discrete) equations that are not in conflict with the discrete nature of matter.

Furthermore, all global quantities are implicitly associated with geometrical objects (lines, areas and volumes). By performing a limit analysis of the mean global quantities, the geometrical content of the global quantities is lost. When we return to a finite formulation, we must reconstruct the lost geometrical content. We are then faced with two processes, one the inverse of the other: from finite to differential and then back to finite. This cumbersome double transformation can be avoided by starting directly from physical laws in finite form, as the CM does. The starting point of this alternative procedure is the use of global variables instead of field functions. Global variables are referred not only to points, but also to lines, surfaces and volumes: they are domain functions and not point functions.

In its first formulation, the linear interpolation, the CM subdivides the domain to study into simplexes, for each of which it is possible to assume that the strain and the stress are uniform and that the material is homogeneous. This hypothesis does not involve any

restriction on the strain-stress analysis, on constitutive laws, or equilibrium conditions:

- the Stokes-Helmholtz theorem, which decomposes the strain into a translation, a rotation, and a pure strain, is valid in a uniform strain region and does not require an infinitesimal region;
- the Cauchy relation, which relates the surface force with the plane surface element by the stress tensor, does not require an infinitesimal region: it's sufficient that the stress in the region is uniform;
- constitutive laws are found experimentally from uniform stress and strain regions, and from homogeneous samples;
- equilibrium is valid in every portion of the body, and not only in infinitesimal volumes.

Consequently, deformation of solids can be studied without resorting to a derivative formulation.

The CM divides the domain by means of two cell complexes, in such a way that every cell of the first cell complex, which is a simplicial complex, contains one, and one only, node of the other cell complex. This procedure establishes a geometrical duality between the two cell complexes.

The duality is extended to equilibrium and congruence analysis: physical variables have a well-defined reference to geometrical objects of the two cell complexes. In particular, configuration variables, geometrical and kinematical, are referred to the objects of the simplicial complex, denoted "primal", while source variables, static and dynamical, are referred to the objects of the other complex, denoted "dual".

The duality can also be extended to the orientations. Indeed, if one assigns to the objects of the primal complex an internal orientation, all objects of the dual complex are automatically endowed with external orientation. Thus, configuration variables are naturally associated with geometrical objects endowed with an internal orientation, while source variables are naturally associated with geometrical objects endowed with an external orientation.

The conservation law is enforced on the dual polygon of every primal vertex. In this respect, the CM corresponds to one of three schemes used in the FVM to choose the control volume [Mavripilis (1995)]: the vertex-based scheme. However, this is the only common factor shared by the CM and the FVM. In fact, the FVM (unlike the CM), evaluates global quantities by integrating differential equations that use field variables, uses mainly one mesh, does not use interpolating functions inside every primal cell, and does not permit free control volumes to be dealt with. Furthermore, it uses mainly structured grids, does not respect flux continuity on the cell faces, and has limited order of accuracy (usually no more than second order) [Morton and Stringer (1995)].

The FDM is also based on a different philosophy from the CM. It starts with a differential equation, in which the derivatives are approximated by difference quotients. This involves the use of a Cartesian mesh, which is one of the principal reasons for the decline of this method in favor of the FEM. Moreover, a concentrated force is difficult to treat numerically using the FDM (unlike the CM).

In general, a concentrated force is difficult to treat numerically for all differential methods. For analysis, the notion of distribution is used, as with the Dirac delta function. However distributions cannot be used in numerical analysis, as the distribution space does not admit a norm.

For a source that is uniformly distributed over the whole domain, the source vector of the FEM is coincident with the source vector of the CM. In this case, it can be shown [Tonti (2001)] that, using linear shape functions on simplicial complexes, the stiffness matrix of the CM is coincident with the stiffness matrix of the FEM. When sources are not uniformly distributed, the CM and the FEM do not provide the same result for the source vector, and, consequently, for the mass matrix in dynamic problems. In fact, in the FEM a concentrated source is distributed to the vertexes according with the "lever rule", whereas in the CM a concentrated source is entirely charged to the dual polygon in which it is located.

3 Implementation of the CM with linear interpolation

Linear interpolation of the CM is obtained by employing affine interpolation functions of the displacement field in every primal cell (§2). The dimensions of primal cells are chosen so that the assumption of uniform strain is accurate. This is the fundamental assumption when using linear interpolation.

As stated in §2, the CM uses two meshes, the one the dual of the other. In this study, a Delaunay/Voronoi mesh generator [George (1995)] is used to generate the two meshes in the two-dimensional domain (Fig. 2). The primal mesh (the Delaunay mesh) is obtained by

subdividing the domain into triangles, so that for each triangle of the triangulation, the circumcircle of that triangle is empty of all other sites. The dual mesh (the Voronoi mesh) is formed by the polygons whose vertexes are at the circumcenters of the primal mesh. The Voronoi diagram has the property that for each site every point in the region around that site is closer to that site than to any of the other sites. Figs. 2 & 3 show the CM association between physical variables and geometrical elements of the two cell complexes (§2). In particular [Nappi, Rajgelj and Zaccaria (1997)], displacement vectors $\underline{u}_i$, $\underline{u}_j$, $\underline{u}_k$ are associated with nodes P_i, P_j, P_k of the A_{ijk} generic primal cell:

$$\underline{u}_q = w_q \underline{e}_x + v_q \underline{e}_y \qquad q = i, j, k . \tag{1}$$

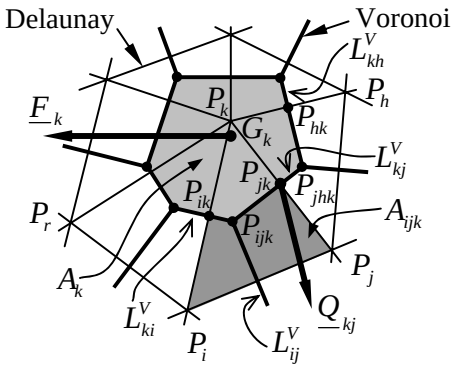

Figure 2: The Delaunay/Voronoi mesh and the association of the Voronoi geometric elements with the source variables

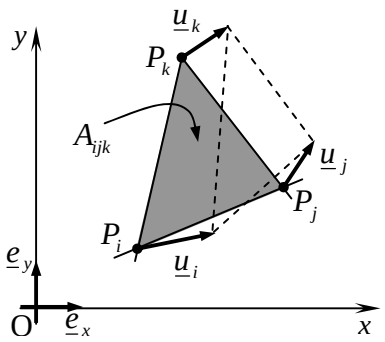

Figure 3: The association of the Delaunay geometric elements with the configuration variables

Relative displacements $\underline{h}_{nm}$ are associated with oriented sides $\underline{L}_{nm} = (P_m - P_n) = \left[\Delta x_{nm} \;\; \Delta y_{nm}\right]^T$:

$$\underline{h}_{nm} = \underline{u}_m - \underline{u}_n \quad (n = i, j, k;\ m = j, k, i). \tag{2}$$

A homogeneous state of strain is associated with the complex of primal cells (§2), represented by the affine transformation related to the nodal displacement components of these cells (Fig. 4).

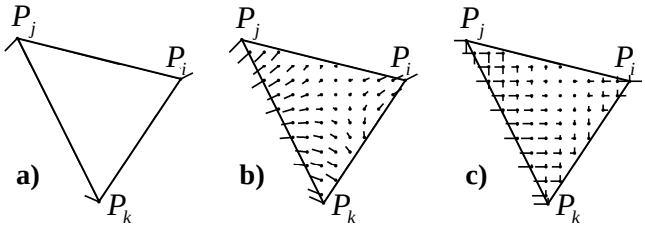

Figure 4: Nodal displacements (**a**), displacement field (**b**), and displacement components (**c**) assuming an affine field

For the nodal displacements shown in a primal cell (Fig. 4a), the hypothesis of an affine displacement field (Fig. 4b) results in the linear behavior shown in Fig. 4c for the displacement components.

The affine transformation can be expressed in the form:

$$\underline{h}_{nm} = \underline{H}_{ijk}\, \underline{L}_{nm}, \quad (n = i, j, k;\ m = j, k, i) \tag{3}$$

where $\underline{H}_{ijk}$, displacement gradient of A_{ijk}, is a double tensor which, in general, is not symmetric.

The determinant of the transformation is:

$$\Delta_{ijk} = \det \underline{H}_{ijk} = \begin{vmatrix} x_i & y_i & 1 \\ x_j & y_j & 1 \\ x_k & y_k & 1 \end{vmatrix}. \tag{4}$$

This determinant is twice the magnitude of the oriented area of A_{ijk}, with its sign (according to the corkscrew rule):

$$\Delta_{ijk} = 2A_{ijk} . \tag{5}$$

Consequently, the determinant can be positive or negative depending upon whether the cell vertices are arranged in an anticlockwise or clockwise sense.

Once known $\underline{H}_{ijk}$, the components of the infinitesimal strain tensor $\underline{\varepsilon} = \left[\varepsilon_x \;\; \varepsilon_y \;\; 2\varepsilon_{xy}\right]^T$ can be immediately evaluated:

$$\underline{\varepsilon} = \underline{B}\underline{u}, \tag{6}$$

where,

$$\underline{u} = \left[w_k \quad v_k \quad w_i \quad v_i \quad w_j \quad v_j\right]^T, \tag{7}$$

$$\underline{B} = \frac{1}{\Delta_{ijk}} \begin{bmatrix} \Delta y_{ji} & 0 & \Delta y_{kj} & 0 & \Delta y_{ik} & 0 \\ 0 & \Delta x_{ij} & 0 & \Delta x_{jk} & 0 & \Delta x_{ki} \\ \Delta x_{ij} & \Delta y_{ji} & \Delta x_{jk} & \Delta y_{kj} & \Delta x_{ki} & \Delta y_{ik} \end{bmatrix}. \quad (8)$$

As stated in §2, the equilibrium equations have to be written for dual cells. Using (Fig. 2) A_k to denote the dual cell whose nodes are P_{ijk}, P_{jhk}, …, and whose oriented sides are $\underline{L}^V_{ik}$, $\underline{L}^V_{jk}$, $\underline{L}^V_{hk}$, …, G_k describes the barycenter of A_k, $\underline{F}_k$ the body force associated with A_k, and $\underline{Q}_{kj}$ the interface force associated with $\underline{L}^V_{kj}$. The equilibrium equations then take the form:

$$\underline{Q}_{kj} = -\underline{Q}_{jk}, \quad (9)$$

$$\sum_j \underline{Q}_{kj} + \underline{F}_k = \underline{0}, \quad (10)$$

$$\sum_j \left(P_{jk} - 0\right) \times \underline{Q}_{kj} + \left(G_k - 0\right) \times \underline{F}_k = \underline{0}. \quad (11)$$

Three oriented lines (for example $\underline{L}_{ij}$, $\underline{L}_{jk}$ & $\underline{L}_{ki}$) are associated with each Voronoi node, (in this case, P_{ijk}). Three interface forces $\underline{Q}_{ij}$ $\underline{Q}_{jk}$ & $\underline{Q}_{ki}$ are associated with these lines. Finally, a state of stress represented by a double symmetric tensor $\underline{\sigma}_{ijk}$ (stress tensor) is associated with the beam of lines passing through P_{ijk}. Thus, it is possible to express each interface force as a function of the two stress tensors associated with the junctions of the corresponding interface:

$$\underline{Q}_{kj} = \underline{\sigma}_{jhk}\, \underline{R}\left(P_{jk} - P_{jhk}\right) - \underline{\sigma}_{ijk}\, \underline{R}\left(P_{jk} - P_{ijk}\right). \quad (12)$$

$\underline{R}$ represents a counter-clockwise rotation by 90°:

$$\underline{R} = \begin{bmatrix} 0 & -1 \\ 1 & 0 \end{bmatrix}. \quad (13)$$

For each A_k dual cell, the following property follows from assuming a uniform stress field (Fig. 5):

$$\begin{aligned} \underline{\sigma}_{ijk}\, \underline{R}\left(P_{jk} - P_{ijk}\right) - \underline{\sigma}_{ijk}\, \underline{R}\left(P_{ik} - P_{ijk}\right) &= \underline{\sigma}_{ijk}\, \underline{R}\left(P_{jk} - P_{ik}\right) \\ &= \frac{1}{2} \underline{\sigma}_{ijk}\, \underline{R}\left(P_j - P_i\right) \end{aligned} \quad (14)$$

By means of Eq.14, the first term in Eq.10 becomes:

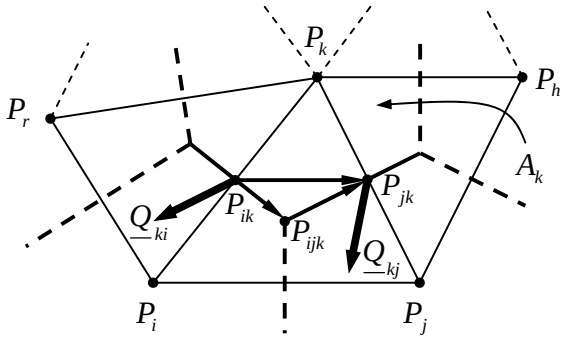

Figure 5: Property of the stress field

$$\sum_j \underline{Q}_{kj} = -\frac{1}{2} \sum_j \underline{\sigma}_{ijk}\, \underline{R}\left(P_j - P_i\right). \quad (15)$$

Eq.10 can then be written as:

$$\frac{1}{2} \sum_j \underline{\sigma}_{ijk}\, \underline{R}\left(P_j - P_i\right) = \underline{F}_k. \quad (16)$$

For cells located on the boundary, Eq.10 takes the form:

$$\sum_j \underline{Q}_{kj} + \underline{Q}_k + \underline{F}_k = \underline{0}. \quad (17)$$

$\underline{Q}_k$ is the interface force to the boundary.

These equations are implemented in the same manner as for FEM:-

– a compatibility equation: Eq.6;

– the constitutive law:

$$\underline{\sigma} = \underline{D}\underline{\varepsilon}. \quad (18)$$

– an indefinite equilibrium equation: by means of Eqs.12, 18, and 6, the interface force can be expressed as a function of displacement:

$$\underline{S} = \underline{R}\underline{L}, \quad (19)$$

$$\underline{N} = \begin{bmatrix} S_x & 0 & S_y \\ 0 & S_y & S_x \end{bmatrix}, \quad (20)$$

$$\underline{Q} = \underline{N}\underline{\sigma} = \underline{N}\underline{D}\underline{\varepsilon} = \left(\underline{N}\underline{D}\underline{B}\right)\underline{u}. \quad (21)$$

By using Eq.10, a linear system of equations can be written for each dual cell, in the form:

$$\underline{F} = \underline{K}\underline{U}. \quad (22)$$

$\underline{F}$ and $\underline{U}$ are the force and displacement vectors respectively, and $\underline{K}$ is analogous to the stiffness matrix

in the FEM, which is symmetric, and defined as positive for properly constrained systems. To assemble $\underline{K}$, the contribution of each primal cell is computed, taking into account the relationship between the local and global node numbering schemes (as in the FEM):

$$\underline{u} = \underline{C}\underline{U} . \tag{23}$$

$\underline{C}$ is a Boolean matrix describing the location of the vertices.

If we consider the dual cell A_k as a prism of unit thickness, the terms $\underline{R}\left(P_{jk} - P_{jhk}\right)$ and $\underline{R}\left(P_{jk} - P_{ijk}\right)$ in Eq.12 are the lateral area of the prism A_k, with regard to the edges $P_{ijk}P_{jk}$ and $P_{ik}P_{ijk}$. This new approach [Tonti (2001)] is more general than the previous approach, since it can easily be extended to three-dimensional analysis.

4 Mesh generator

The following are the main features of EasyMesh, the freeware mesh generator for generic domains used in this study. EasyMesh:-

- generates two dimensional, unstructured, Delaunay and constrained Delaunay triangulations;
- can handle holes in the domain;
- can easily describe local refinement / coarsening of the mesh;
- handles domains with more than one material;
- performs re-numbering of nodes, elements and sides, to decrease the bandwidth of the equations;
- has a built-in function for relaxation of the grid, to avoid creating nodes surrounded by more than 7 and less than 5 elements;
- performs Laplacian smoothing;
- generates an adaptive mesh: for each node the desired side length can be specified for the triangle containing that node in the final triangulation.

Fig. 6 shows an example of a domain with several materials and a hole, requiring refinement of the mesh in some regions, and coarsening of it in others.

Points 0-1-3-9-8-11-10-7-6-2 define the boundary of the domain and represent a boundary chain. They must be inserted in an anticlockwise sense.

Points 16-17-18-19 define the hole and represent a hole chain. They have to be inserted in a clockwise sense.

Smaller or larger elements can be specified for particular regions inside the domain by using “false holes”. In Fig. 6, points 20-21-22-23 define the false hole used to refine the grid in that region. They must be inserted in an anticlockwise sense, as for the domain boundaries.

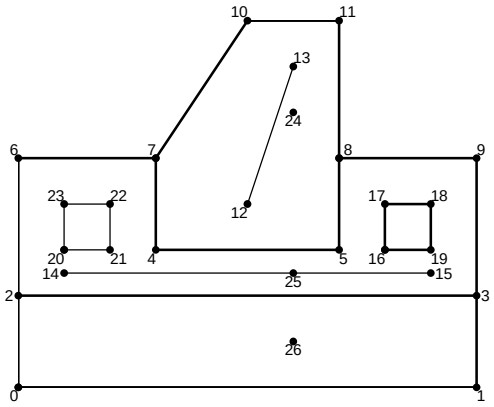

Figure 6: Domain to be meshed

Points 2-3 and 7-4-5-8 define the interfaces between regions with different materials. Points 24, 25 and 26 are used to assign materials to specific regions.

Points 12-13 and 14-15 define interior lines, to describe coarsening of the mesh.

The mesh generated by the mesh generator is shown in Fig. 7.

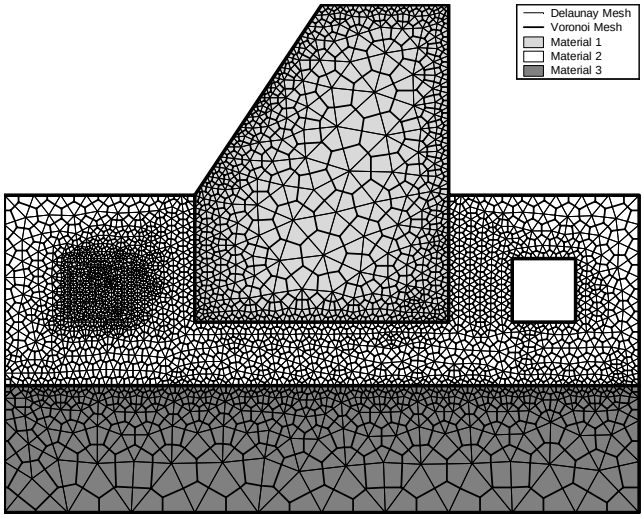

Figure 7: Meshed domain

EasyMesh is the first mesh generator studied for numerical applications with the CM. Its simplicity makes it very easy to use. Nevertheless, it is susceptible to problems generating the mesh near the boundary of non-convex domains. For these cases, the

user must specify an accurate choice of side length of the triangles. This could be a difficult problem for automatically remeshing crack propagation problems. Other Delaunay/Voronoi mesh generators are being considered at the moment. The CM has recently been implemented for barycentric dual mesh and meshless methods [Zovatto(2001)].

5 Computing the crack propagation direction

The crack propagation direction can be determined using a variety of criteria:

- the maximal normal stress criterion [Erdogan and Sih (1963)];
- the maximal strain criterion [Maiti and Smith (1984)];
- the minimum strain energy density fracture criterion [Sih and Macdonald (1974), Sih (1981), Carpinteri and Sih (1984), Sih (1985)];
- the maximal strain energy release rate criterion [Paris and Erdogan (1963)];
- the damage law criteria [Koenke and Schmid (1997)].

In the present paper, the crack propagation direction is derived directly from the properties of the Mohr's pole [Di Tommaso (1981)]. If σ and τ are the normal and shear components, respectively, of the stress acting on a general Voronoi side, the Mohr-Coulomb criterion predicts that crack propagation occurs if:

$$|\tau| = c - \sigma \tan\varphi \,. \tag{24}$$

c and φ are material properties. In Eq.24, compressive actions are defined as negative.

The direction of propagation can only be found if the Mohr's circle representing the stress field in the neighborhood of the tip is known. Crack propagation occurs when this circle is tangent to the limit surfaces in the Mohr-Coulomb plane. Thus, to apply the Mohr-Coulomb criterion, the stress field in the neighborhood of the tip must first be determined. The CM association between dual geometrical objects and source variables (§2) is used in this study to determine the stress field.

To take advantage of this association, the shape of the primal (Delaunay) mesh surrounding the tip is fixed beforehand, so that the mesh generator generates an almost regular Voronoi polygon centered on the crack tip [Ferretti, Viola, Di Leo and Pascale (1999)]. In the remainder of the domain, the mesh generator is allowed to generate the mesh automatically.

5.1 Crack tip mesh

The dual mesh around the tip is created as follows:-

- the input file for the mesh generator, which defines the geometry of the domain, is modified to add six new nodes representing the vertexes of a regular hexagon centered on the tip;
- the desired element dimension (§4) for the six new nodes and for the tip node is set equal to the side of the regular hexagon;
- the input file for the mesh generator is modified to add seven new sides which join the six new nodes and the crack tip node in a counter-clockwise sense, without crossing the surfaces of the crack;
- a marker is associated with the seven new sides, indicating that the polygon that starts and ends with the crack tip node, and touches all six of the new points, is a false hole (§4).

This false hole will be termed the "first hexagonal kernel".

For the case shown in Fig. 8, the first hexagonal kernel has been inserted so that one of its nodes lies on an edge of the crack.

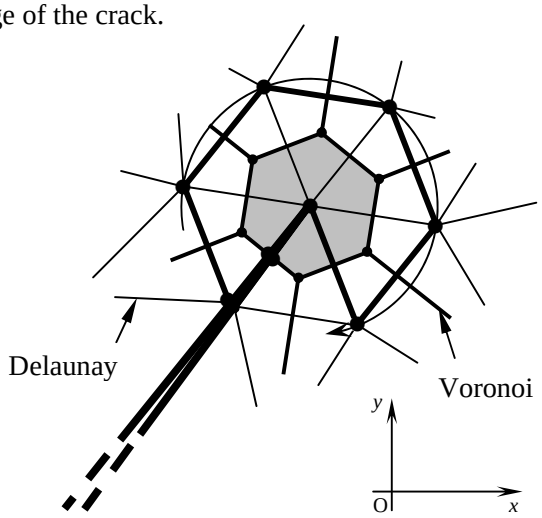

Figure 8: First hexagonal kernel at the crack tip

EasyMesh treats the boundary chain of a false hole as a closed internal interface between two parts of the domain. Usually, a false hole is used to refine the grid in a particular region of the domain (§4). In the present paper, it is used to specify a particular mesh geometry in a region, for use by the mesh generator.

Once the mesh generator has been activated, it creates a Delaunay mesh that divides the first hexagonal kernel into five equilateral triangles. This happens because the desired element dimension chosen for the 7 vertexes of

the first hexagonal kernel is equal to the hexagonal kernel side.

Dividing the first hexagonal kernel into equilateral elements resembles the ring of elements surrounding the tip of the crack used in FEM. However, the aim is different: in the FEM the radial concentric mesh around the crack tip allows the asymptotic development of the stress field at the crack tip. Sih, DeLorenzi and German (1976), Barsoum (1974, 1976), Henshell and Shaw (1975) and Harrop (1985) demonstrated analytically the singularity in stress (required for linear elastic fracture mechanics - LEFM) can be realised by distributing the intermediate nodes of isoparametric finite elements in a non-uniform manner. Specific elements for treating the singularity at a crack tip were developed from 1968 onwards [Sih and Liebowitz (1968), Benzley and Beisinger (1973), Benzley (1974)].

The Voronoi polygon centered on the crack tip, required for the CM, is the gray-shaded polygon shown in Fig. 8. This polygon will be termed the "crack tip Voronoi cell". Due to the way it is constructed, four of its sides are positioned equidistant from the crack tip, which belong to a hexagon centered on the crack tip, termed the "second hexagonal kernel". These sides join the circumcenters of the five equilateral triangles.

A simple geometric relationship exists between the sides of the first and second hexagonal kernels, named l^I and l^{II}, respectively:

$$l^{II} = \frac{\sqrt{3}}{3} l^I \tag{25}$$

5.2 Positioning the first hexagonal kernel

In this work, two input files are used to study crack propagation through a domain.

The first input file defines the current geometry of the domain. It has to be modified every time crack propagation occurs. The first input file is not, properly speaking, an input file, since the mesher works from the second input file.

The second input file is derived from the first input file, with the addition of the nodes and internal sides that define the first hexagonal kernel (§5.1). When generated numerically, the first hexagonal kernel is initially positioned on the origin of the reference frame, as shown in Fig. 9. Next, the first hexagonal kernel is moved from the origin to the crack tip. As it is translated, it is also rotated, so that it takes up one of the two positions described in §5.4, taking care that it does not cross the crack (Fig. 8). To achieve this, crack tip coordinates and the direction of the last portion of the crack must be computed.

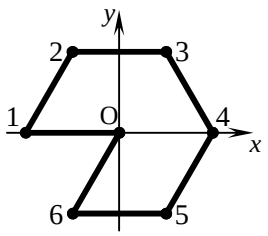

Figure 9: Generation of the first hexagonal kernel

Once the coordinates of the transformed first hexagonal kernel have been calculated, the second input file can be derived from the first input file by updating the node and edge numbering, remembering that nodes defining a false hole chain must be inserted in a clockwise sense (§4). Furthermore, the addition of nodes and sides defining the first hexagonal kernel modifies the sequential numbering of those nodes and sides defining the domain geometry. A special tool has been developed to ensure that the second input file is correctly written. This tool re-writes the second input file twice, once for each of the desired positions of the first hexagonal kernel (§5.4). For every modification to the second input file, the mesh generator is automatically invoked again.

5.3 Analysis in the Mohr-Coulomb plane

The force acting on the Voronoi side *a* has the same components in the (*x*,*y*) global reference frame, $\underline{Q}_a^V = \left[Q_{a_x}^V \; Q_{a_y}^V \right]^T$, as in the $(\bar{x}, \bar{y})$ local reference frame, $\underline{\bar{Q}}_a^V = \left[Q_{a_{\bar{x}}}^V \; Q_{a_{\bar{y}}}^V \right]^T$ (Fig. 10).

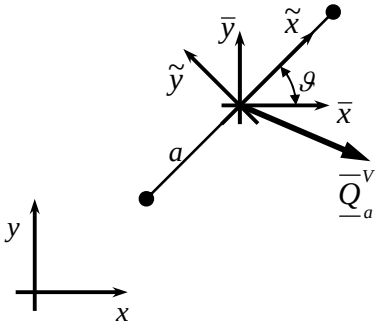

Figure 10: Global and local reference frames for a general Voronoi side *a*

Denoted the angle between the Voronoi side and the *x* axis as ϑ (Fig.10), the force $\underline{\overline{Q}}_a^V$ can be projected perpendicular and parallel to the Voronoi side, using the matrix $\underline{T}_a$:

$$\underline{T}_a = \begin{bmatrix} \cos\vartheta & sin\vartheta \\ -sin\vartheta & \cos\vartheta \end{bmatrix}. \tag{26}$$

This gives $\underline{\tilde{Q}}_a^V = \left[Q_{a_{\tilde{x}}}^V \; Q_{a_{\tilde{y}}}^V \right]^T$, the projection of $\underline{\overline{Q}}_a^V$ in the $\tilde{x}/\tilde{y}$ local reference frame:

$$\underline{\tilde{Q}}_a^V = \underline{T}_a \underline{Q}_a^V . \tag{27}$$

Finally, to obtain the vector whose components are the normal and the tangential stress on *a*, $\underline{t}_a^V = \left[\tau_a^V \sigma_a^V \right]^T$, $Q_{a_{\tilde{y}}}^V$ and $Q_{a_{\tilde{x}}}^V$ must be divided by l_a, the length of the Voronoi side:

$$\underline{t}_a^V = \frac{1}{l_a} \underline{\tilde{Q}}_a^V . \tag{28}$$

Rotating the first hexagonal kernel around the crack tip, and plotting the points whose coordinates are derived from Eq.28 on the Mohr-Coulomb plane, the projection of the stress field onto the sides of the crack tip Voronoi cell is obtained.

An example of the stress field representation obtained in this way is shown in Fig. 11 [Ferretti (2001)], which refers to a grade-by-grade clockwise rotation of 59°, starting from the first hexagonal kernel position shown in Fig. 8.

In Fig. 11, a well-defined Mohr's circle can be recognised, together with some dispersed points. The circle is obtained by rotation of the crack tip Voronoi cell sides that are equidistant from the tip, as these lie on the second hexagonal kernel. The distance of these sides from the crack tip, *r*, equals the apothem of the second hexagonal kernel:

$$r = \frac{\sqrt{3}}{2} l^{II} = \frac{1}{2} l^I . \tag{29}$$

If the stress field is known for 60 different rotations of the first hexagonal kernel, then this can be extended to define the stress field for a 360° rotation of attitude around the crack tip. The 360° rotation around the crack tip is accompanied by two rotations around the Mohr's circle.

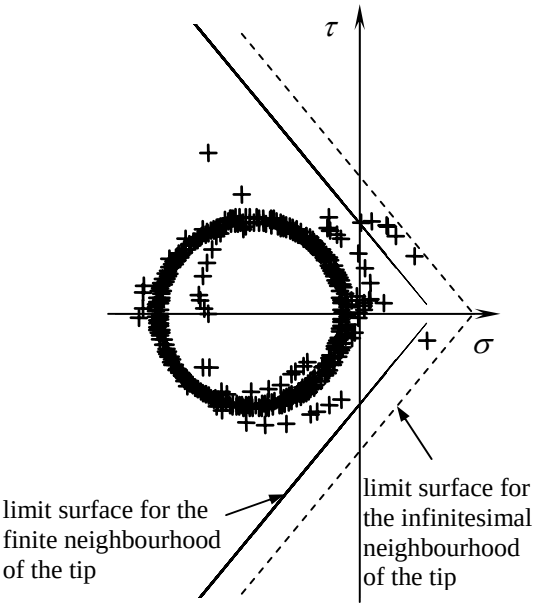

Figure 11: Representation of the stress field in the Mohr-Coulomb plane

The points outside the Mohr's circle correspond to the stress on the crack tip Voronoi cell sides that do not lie on the second hexagonal kernel. These points do not belong to the same crack tip neighborhood as that which the points corresponding to the sides equidistant from the crack tip belong. Thus, in the Mohr-Coulomb plane, the outlying points, termed the "points of type a", should not to be plotted with the points corresponding to the sides lying on the second hexagonal kernel, termed the "points of type b".

Plotting only the points of type b, it is possible to describe the stress field on those attitudes of the tip finite neighborhood whose trace belongs to the plane containing the crack.

Moreover, by varying the value of l^I it is possible to describe the stress field on those attitudes lying on finite neighborhoods of a given dimension.

For a crack whose shape does not vary normal to the plane of the mesh, the direction of crack propagation will always lie in the plane of the mesh. If this is the case, it is not necessary to construct the complete Mohr's domain, but only the Mohr's circle obtained rotating the first hexagonal kernel, since this is the biggest in the Mohr's domain. Therefore, to obtain the crack propagation direction for the case where the Mohr's circle is tangential to the limit surface, it is sufficient to calculate the point in the Mohr-Coulomb domain which lies on the limit surface, and the corresponding direction of the Voronoi side.

Since the simulation proceeds using finite increments of displacement, it is not possible to capture the precise instant for which the Mohr's circle becomes tangent to the limit surface. In general, it is only possible to find the first value of displacement for which the Mohr's circle intersects the limit surface. For this case, the crack propagation direction can be found by calculating the direction of the Voronoi side corresponding to that Mohr's point which lies furthest outside the limit surface.

The limit surface (Eq.24) describes failure in the infinitesimal neighborhood of the crack tip. However, the stress field is calculated at a finite distance from the crack tip. Thus, Eq.24 must be modified, by introducing a correction factor *k*, which is applied to the cohesion, *c*:

$$|\tau| = kc - \sigma \tan\varphi\,, \tag{30}$$

where:

$$k < 1\,. \tag{31}$$

That is to say, the position of the Mohr's circle is studied in a reduced domain, with respect to a translated limit surface (Fig. 11).

5.4 Further remarks

To construct the Mohr's circle it is sufficient to know any two points in the Mohr-Coulomb plane, and consequently it is sufficient to know the stress field on two attitudes of the same (finite) neighborhood. Remembering that only the sides of the tip Voronoi cell that lie on the second hexagonal kernel need to be taken into account (§5.3), for a general position of the first hexagonal kernel only three distinct attitudes are available. Of the four sides belonging to the second hexagonal kernel (Fig. 8), two of them are parallel to each other, and correspond to the same attitude. So, one generic position of the first hexagonal kernel is sufficient to identify the circle.

Nevertheless, the uncertainty of the first hexagonal kernel orientation cannot guarantee a good accuracy during numerical solution. It has been found [Ferretti (2001)] that the accuracy is not satisfactory for side slopes near to 0° and 90°.

A numerical analysis [Ferretti (2001)] showed that higher accuracy solutions are obtained for side slopes close to 30° and 60°. Since the difference between the slopes of two consecutive sides of the second hexagonal kernel is equal to 60°, it is impossible to insert a first hexagonal kernel giving the higher accuracy solution for at least two sides of the hexagon.

Thus, to identify the Mohr's circle, two different orientations of the first hexagonal kernel can be used. For the first of them (Fig. 12a) a Voronoi side slope of 60° is available, while for the second (Fig. 12b) a Voronoi side slope of 30° is available.

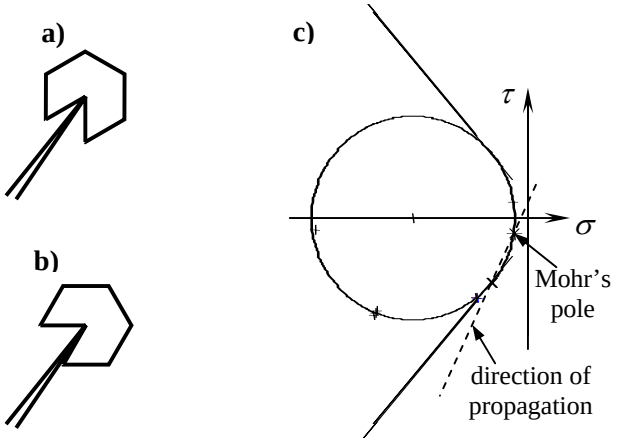

Figure 12: a), b) First and second positions of the first hexagonal kernel; **c)** Computed Mohr's circle

To optimize computation, only the positive/negative slope needs to be taken into account. Due to the properties of the Mohr circle, slopes with the same sign are sufficient to uniquely identify it. In Fig. 12c, only the stress points relating to positive slopes have been plotted. These points refer to sides rotated by 30° relative to one another. Thus, the angle measured from the centre of the Mohr's circle to each of these points is 60°. This information is sufficient to calculate [Ferretti (2001)]:

- the radius *R* of the Mohr's circle;
- the position of the Mohr's circle center;
- the distance *d* between the Mohr's circle center and the limit surfaces;
- the position of the Mohr's pole.

The condition for no crack propagation takes the form:

$$d > R\,. \tag{32}$$

When $d \le R$, the code automatically calculates:

- the position of the point on the Mohr's circle, which minimizes the distance between the Mohr's circle and the limit surface;
- the crack propagation direction, given by the direction of a line that joins the above critical point to the Mohr's pole (Fig. 12c).

6 Crack geometry uploading

It has already been stated (§5.3) that the simulation in this paper proceeds by finite increments of the displacement value.

If the condition for no crack propagation (Eq.32) is not satisfied for a general loading step, the length of crack propagation is assumed equal to the length of a side of the first hexagonal kernel (§5.1). This side length is a parameter in the numerical simulation and is input by the user.

Once the direction of crack propagation has been determined by the method described in §5.4, the crack geometry is updated by modifying both the first and second input files:

- Step 1: a new edge representing the crack propagation is added (by modifying the first input file);
- Step 2: the first hexagonal kernel is moved from the old to the new crack tip (by modifying the second input file).

For the first step, two new nodes and two new sides are added to the first input file (Fig. 13).

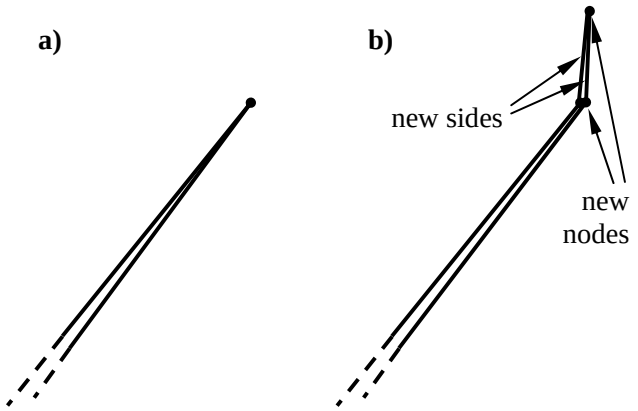

Figure 13: a) Old crack; **b)** New crack

The first of these new nodes is the new tip, while the second added node describes the separation of the crack surfaces at the old crack tip. The two added sides join the new crack tip to the two nodes at the former crack tip.

A special tool has been developed to update the first input file automatically when Eq.32 is not satisfied.

In the second step, the first hexagonal kernel is moved by updating the value of the crack tip coordinates and the slope of the last portion of the crack. The first hexagonal kernel is then created and moved as described in §5.2.

At this point, the mesh generator is automatically invoked again and a new mesh is generated for the new crack geometry.

Next, the Mohr-Coulomb stress analysis is repeated in the finite neighborhood of the new crack tip, without incrementing the displacement value. If Eq.32 is not yet satisfied, further crack propagation occurs, accompanied by updating of the crack geometry. The crack is allowed to grow until it is stable (when Eq.32 is satisfied). At this point, the value of displacement is incremented and the condition for no crack propagation re-evaluated.

Due to the way the crack is extended, pairs of nodes are positioned opposite each other on the crack surfaces.

This technique is mesh-independent, since the direction of propagation is computed independently of the mesh (by intra-element propagation). It requires a remeshing stage at each step of propagation, but results are very accurate.

To decrease the number of required remeshing stages, an inter-element propagation technique can be followed, which assumes that the final direction of crack propagation is the triangle side nearest to the computed direction of propagation [Bouchard, Bay, Chastel and Tovena (2000)], giving crack propagation along the edges of triangles. This technique is mesh-dependent, but it does not require a remeshing procedure, since the extension of the crack is described only by nodal relaxation. However, the method is inaccurate and needs an initially fine mesh. Indeed, to accurately model the large stress concentration at the crack tip, an infinitely fine mesh is required. The crack propagation along the edges of triangles results in frequent changes in the crack propagation direction. To improve the precision at the crack tip, a remeshing procedure can be used in addition to nodal relaxation at the crack tip. However, this type of propagation involves large modifications to the local stress field. In complex domains these modification to the stress field can lead to inaccurate propagation paths, as crack bifurcation can occur due to the imposed direction, so that the crack follows multiple paths. In summary, inter-element propagation is faster than intra-element propagation, but it is less accurate.

7 Mixed-mode crack propagation

Mixed-mode crack propagation occurs when the load is applied obliquely to the crack direction and the crack opening direction (Fig. 14).

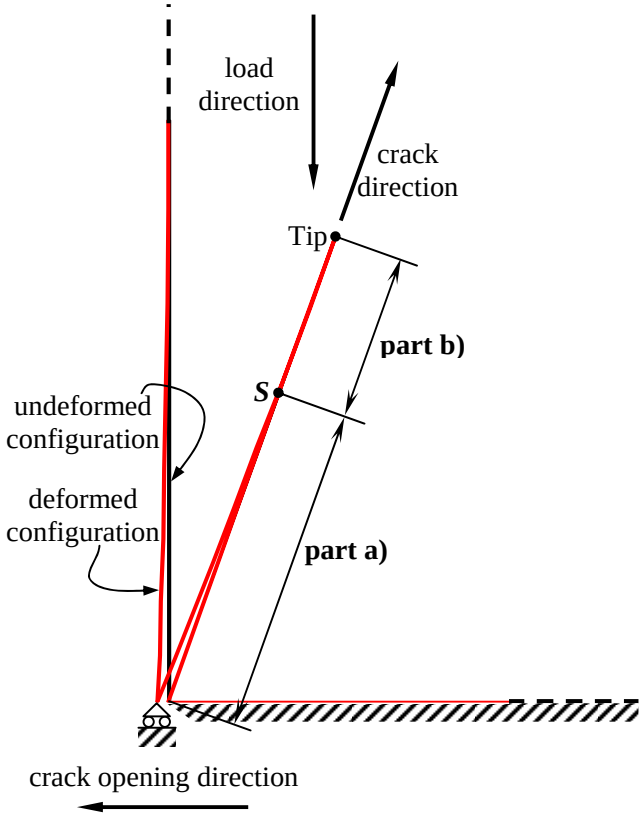

Figure 14: Mixed-mode crack loading

In this paper, only the combination of the Mode I and Mode II cases is considered. For this combination, when a crack is subjected to mixed-mode loading, it can be divided into two parts [Ferretti (2001)]:

part a) Mode I prevails and the two edges of the crack separate;

part b) Mode II prevails and the two edges of the crack slide over one another.

Depending upon the geometry of the domain and the boundary conditions, there may be more than one part a) and more than one part b). Generally speaking, part b) occurs whenever the combination of loading and boundary conditions forces the edges of the crack to close at some point.

The part a) and part b) are shown in Fig. 14 for the case of a crack with a general inclination, in which the mouth of the crack is constrained in the horizontal direction.

Numerical simulation is only possible if the position of the point ***S*** separating the two parts is known. The dominance of mode I rather than mode II crack propagation involves different boundary conditions on the crack surfaces, and it is necessary to specify all the boundary conditions before the simulation starts. In general, ***S*** is a function of the load step and crack length, and is, thus, an unknown of the mixed-mode problem. To determine ***S***, it is necessary to proceed step-wise:

Step I) Evaluate the deformed configuration of the domain, by assuming free displacement all over the crack (giving the step I deformed configuration);

Step II) Use the step I deformed configuration to find the part b) extension, by assuming zero relative displacement between opposing nodes lying in part b) (giving the step II deformed configuration);

Step III) Introduce relative displacement between the opposite nodes lying in part b), and re-evaluate the extension of part b) (giving the final deformed configuration).

Step III involves introducing FEM contact elements describing sliding contact [Har (1998), Papadopoulos, Jones and Solberg (1995), Zhong (1995)].

A more detailed description of the steps necessary to determine the position of ***S*** follows.

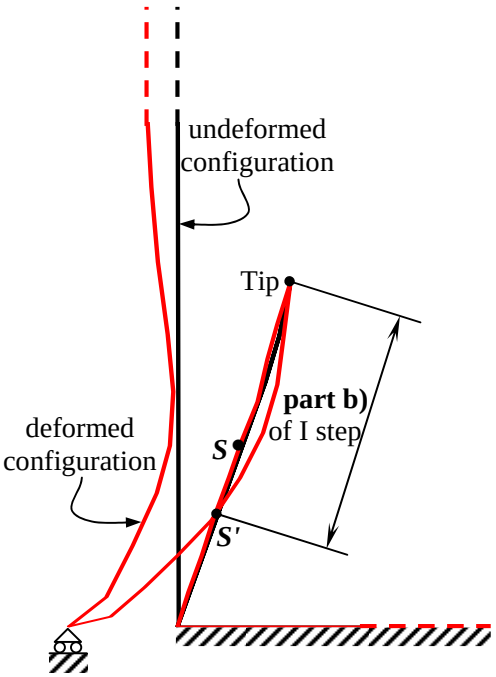

Figure 15: Deformed configuration of the crack after Step I

In the first step (Fig. 15), all nodes lying on the crack are free to move, independent of any displacement constraint relative to the opposite crack edge. Hence, no force acts on the nodes lying on the crack. In part b), this involves penetration of the nodes below the

opposite crack surface. Depending upon the geometry of the domain, and the boundary conditions, it is also possible that some nodes lying in the part a) may penetrate below the opposite crack surface. Thus, the point $\boldsymbol{S'}$ separating the part a) and the part b) portions of the crack does not generally coincide with $\boldsymbol{S}$ after Step I. The position of the point $\boldsymbol{S'}$ defines the extent of part b) after step I.

During the second step, the penetration is eliminated, and the extent of part b) adjusted.

If only one part a) and one part b) occurs along the crack, (as is the case in Fig. 15), the second point which defines the part b) with $\boldsymbol{S}$ is known. It always coincides with the tip. Penetration of the nodes into the opposite crack surface must be adjusted starting from a point that belongs to the actual part b). If the crack contains only one part a) and one part b), penetration has to be adjusted from the node at the other end from point $\boldsymbol{S'}$, since it is not known whether the point $\boldsymbol{S'}$ does indeed belong to the actual part b). (In Fig. 15, elimination of the penetrating nodes occurs from the tip).

A special tool has been developed to eliminate the penetration of nodes between crack surfaces for the case where only one part a) and one part b) exist. This tool examines all the nodes along the same surface of the crack lying in part b) after step I, starting from the node at the other end from point $\boldsymbol{S'}$. At each node, the program checks to see whether penetration occurs. If this is the case, the current node is constrained to have the same displacement components of the opposite node on the crack (§6).

By specifying equal displacements to the nodes on either side of the crack, a constraint in correspondence of the current node is introduced. The reaction forces due to the imposed constraint are applied to the opposite node by change of their sign. These applied forces cause the opposite surface of the crack to deform and, thus, affect the displacement components of the opposite node. To ensure that the paired nodes have the same displacement components (and to re-assess the constraint reactions), the displacement components of the current node must be adjusted until a stable solution is reached.

Every time the boundary conditions of a crack node are changed, the tool re-evaluates the extent of part b), and re-examines all the nodes lying in part b), starting from the node at the opposite end to the revised point $\boldsymbol{S'}$. Every change in boundary conditions involves a change in the extent of part b), and hence a change in the number of nodes lying in part b).

After changing the boundary conditions of a general node lying in part b), it is possible that a node which has previously been examined may become subject to tensile stress. The constraint at this node may no longer be required, due to the introduction of a new constraint at the current node.

For this reason, after re-evaluating the extent of part b) the tool controls whether a node is in traction. If so, deformation constraint at the nodes in tension are relaxed and the extent of part b) is re-evaluated.

Step II gives a deformed configuration that clearly shows the subdivision of the crack into part a) and part b). The point separating these two parts, $\boldsymbol{S''}$, is not yet the actual point $\boldsymbol{S}$, as it does not consider the slip between opposite nodes lying in part b).

Step III estimates the components of relative slip between opposite nodes lying in part b).

A friction model is used to assess the forces acting across the crack surfaces. Relative slip can only take place if the constraining reaction forces for nodes in part b) lie on the surface of the friction cone (Fig. 16).

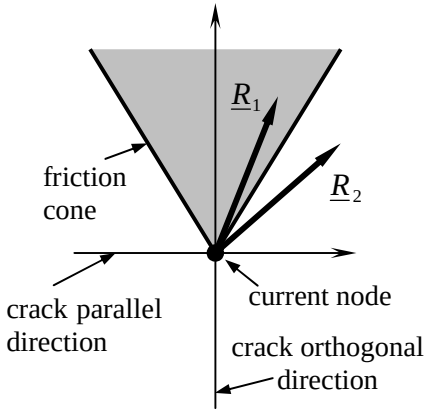

Figure 16 : Example of the validity ($\underline{R}_1$) and of non-validity ($\underline{R}_2$) of the no relative slip assumption

In Fig. 16, $\underline{R}_1$ is a constraint reaction that lies inside the friction cone. For this case, the constraint condition adopted for the current node in step II is correct and no relative slip occurs between it and the node on the opposite crack surface. $\underline{R}_2$ is a constraint reaction that lies outside the friction cone. In the adopted model, reactions lying outside the friction cone cannot exist. Thus, the constraint condition adopted at the current node in step II is not correct, and relative slip will occur between it and the node on the opposite crack surface. The correct value of relative slip results in a reaction that lies upon the conical surface.

The following steps are used to estimate the value of relative slip:-

- An assumed slip is considered at the current node (the first approximation relative slip).
- The new constraining reaction force is evaluated (giving the second approximation of constraining reaction force).
- If the second approximation constraining reaction force lies outside the friction cone, the first approximation relative slip is smaller than the actual slip. Thus, the relative slip is doubled (giving the second approximation relative slip).
- If the second approximation constraining reaction force lies within the friction cone, the first approximation relative slip is greater than the actual slip. Thus, the relative slip is halved (giving the second approximation relative slip).
- The preceding steps establish upper and lower bounds on the relative slip. Interval halving is used to determine the correct slip, for which the upper and lower bounds are equal (to within a particular tolerance).

The common value of the upper and lower bounds is used as the actual value of relative slip.

The node with the maximum angle between the constraining reaction force and the normal to the crack surface is considered first when calculating the relative slip. When relative slip is introduced at the current node, the constraint reactions force at the other nodes will change. Three cases can occur:

1. a constrained node may become subject to tension;

2. a constraint reaction may move to outside from the friction cone;

3. a node lying in part a) during step II may penetrate the opposite crack surface.

Every time a value of relative slip is calculated, the tool checks whether one of these cases has occurred. If this is the case, the process is repeated with the appropriate modifications. In subsequent iterations, the tool remembers the relative slips that have previously occurred along the crack: the same relative slip is maintained between the nodes in part b), so long as the constraint reaction force does not move to outside the friction cone. This allows the energy dissipation associated with each value of relative slip to be estimated.

Finally, the tool also remembers the relative displacements between nodes in part a). In particular, it remembers the relative displacements in the crack direction. If a node lies within part a) for a given imposed displacement, and lies in part b) for the next value of imposed displacement, the relative displacement in the direction normal to the crack surface goes to zero, while the relative displacement in the direction of the crack does not change. Thus, the assumption of zero relative slip during step II may be very far from the truth. Consequently, the simulation may not converge. The tool avoids this problem by modifying the step II constraint conditions for all iterations after the first. Nodes that penetrate the opposite crack surface are constrained to have the same displacement component in normal to the crack surface and to dist in the crack direction by the same relative displacement as in the previous iteration.

8 Numerical results

The procedure described above for identifying the direction of crack propagation has been used to model tests on beams under symmetric and skew-symmetric four point bending [Ferretti, Viola and Di Leo (2000); Ferretti (2001)] and on compressed cylindrical specimens [Ferretti, Viola, Di Leo and Pascale (1999)] (Fig. 17). Both the bending and compressive tests have been performed for concrete specimens.

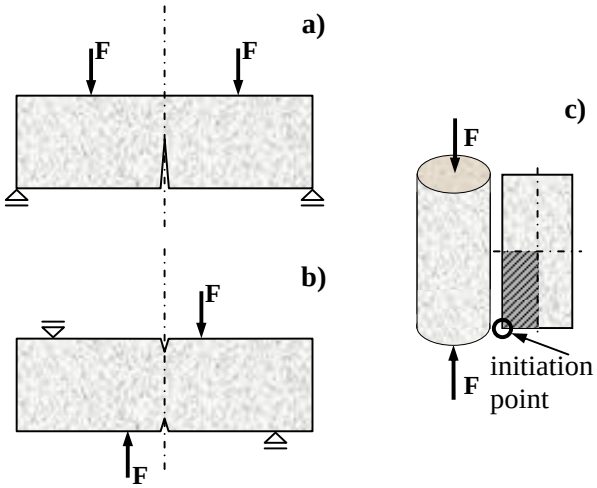

Figure 17: Schematic view of **(a)** the symmetric bending test, **(b)** the skew-symmetric bending test, and **(c)** the compressive test

In the beams under symmetric four point bending, the cracks are subjected to mode I loading, in the beams under skew-symmetric four point bending, the cracks are subjected to mode II loading, and, in cylinders, cracks are subjected to mixed-mode loading.

Experimental observations show that, in the beams under symmetric four point bending, cracks initiate at the mid-span (Fig. 17a) and propagate perpendicularly to the moment vector, in the beams under skew-symmetric four point bending cracks initiate at the mid-span (Fig. 17b) and propagate towards the external load, and, in cylinders, cracks initiate on the curved surface, on the two end caps (Fig. 17c), and propagate through the cylinder. The load at which the cracks initiate is critical in numerical simulations of FM. Most FEM codes of FM are applied to pre-cracked test parts. In particular, it is difficult to determine where the crack will start, since the material is never perfect. Micro-failures and inclusions always induce local stress concentrations, from which failure and cracks originate. These defects cannot realistically be taken into account numerically in large-scale models. Consequently, we must either assume the material to be perfect or impose the point of crack initiation by pre-cracking the specimen. The specimens in this study are also pre-cracked, both for mode I, mode II, and mixed-mode loading. However, a critical stress criterion for determining the location of crack initiation is being studied at the present time.

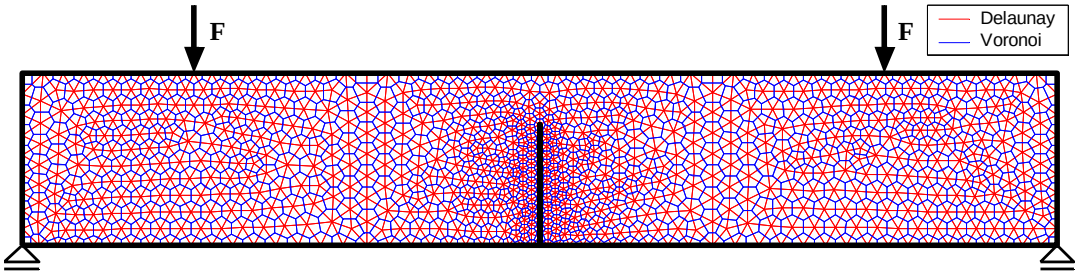

Figure 18: Numerically-calculated crack path for a beam under symmetric four-point bending

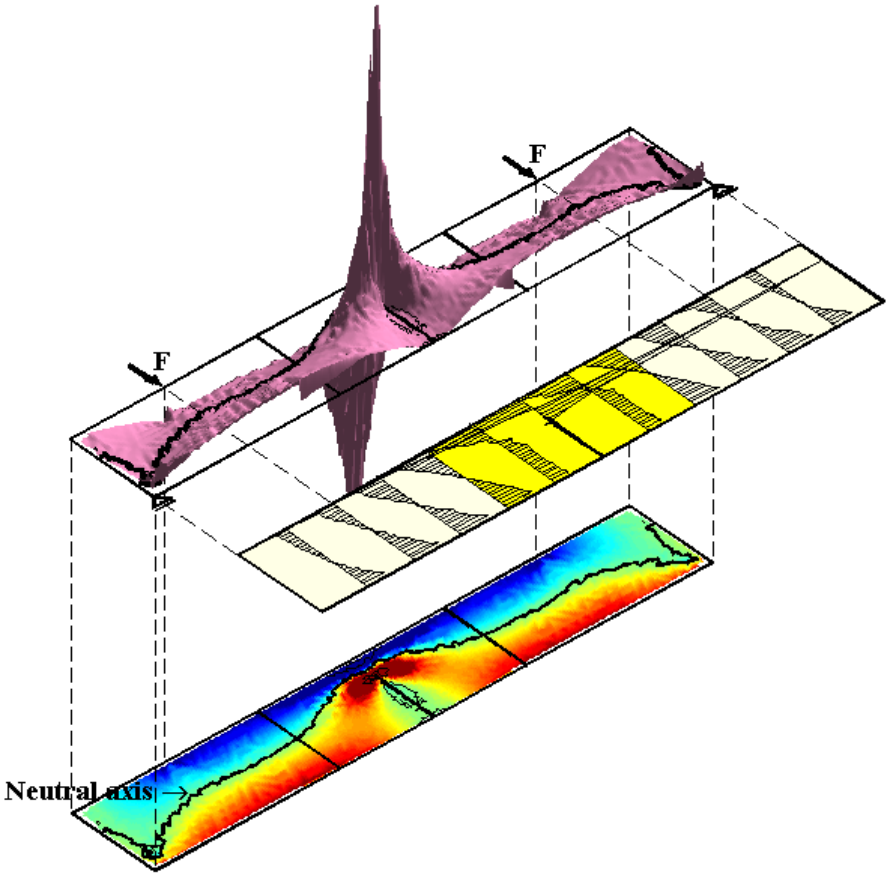

Figure 19 Numerically-calculated stress field in the direction of the beam axis for symmetric four-point bending

For the beams under symmetric four point bending, the crack has been initiated at the bottom-fiber of the mid-span section. The dimensions of the pre-cracking have been fixed in such a manner that they do not significantly modify the stress field around the initiation point.

The computation was performed for only one half of the beam shown in Fig. 17a, due to the presence of an axis of symmetry. The static analysis has been performed on the middle longitudinal section.

Starting from the initiation point, the numerical model predicts near-vertical crack propagation at every stage. The intra-element propagation technique and the possibility to reduce the dimension of the mesh near the tip as small as possible have permitted the crack path to be accurately predicted (Fig. 18).

In Fig. 19, the numerically-calculated stress field in the direction of the beam axis is plotted, both with a discrete 2D representation, a continue 2D representation, and a continue 3D representation.

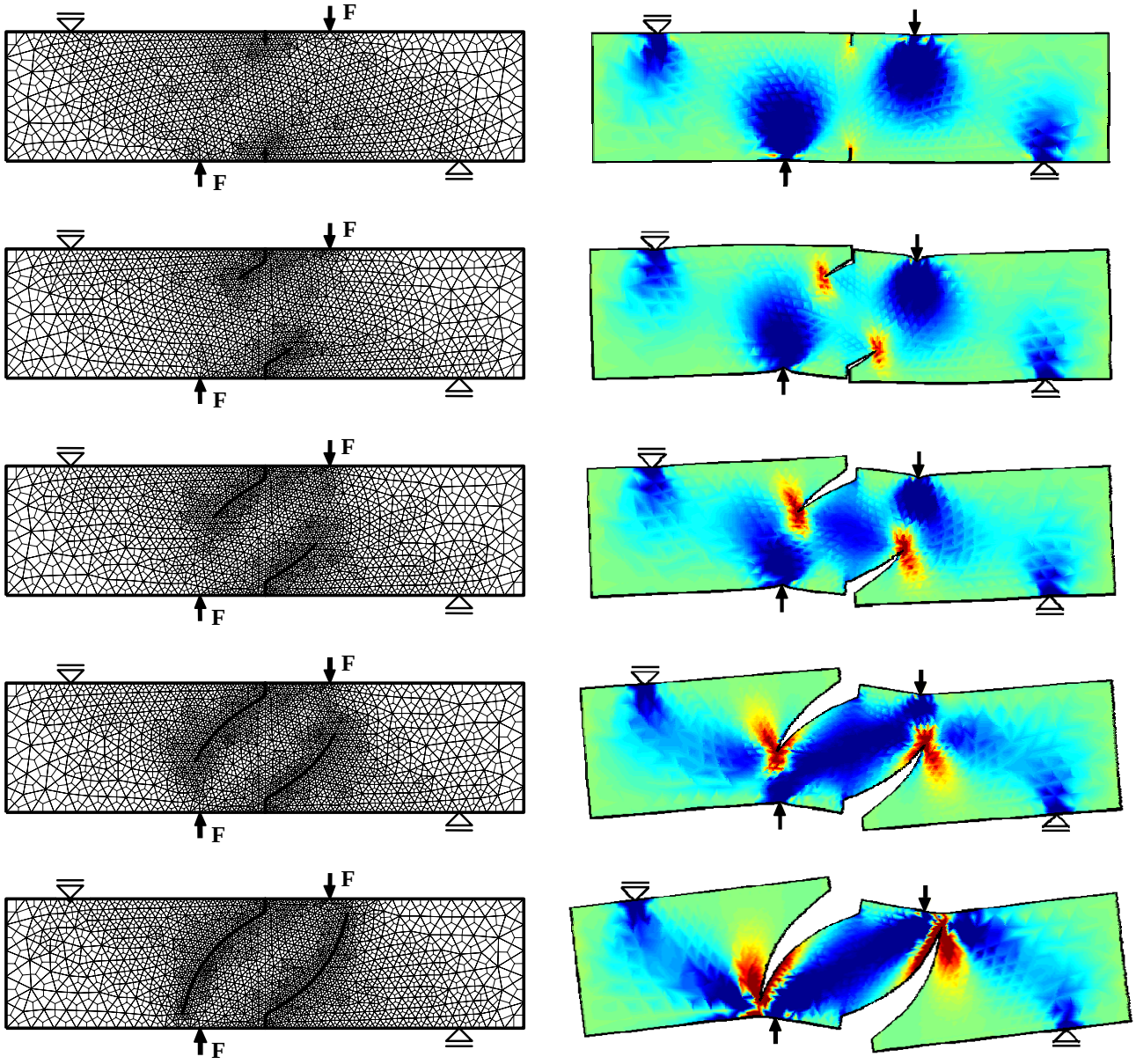

Figure 20: Numerically predicted crack path and stress analysis for five failure stages in a beam under skew-symmetric four point bending

As regards the beams under skew-symmetric four point bending, the crack has been initiated both at the bottom- and at the top-fiber of the mid-span section. In this case too, the dimensions of the pre-cracking have been fixed so as not to modify the stress field around the initiation point significantly.

The skew-symmetry of the displacement field was taken into account in order to simplify the computation. The static analysis has been performed on the middle longitudinal section.

The numerical crack path and the stress analysis predicted by the numerical model are shown in Fig. 20 for five failure stages. In accordance with the experimental evidence, the direction of propagation changes at every stage, in such a way that the numerical crack propagates towards the applied load. Even in this case, the intra-element propagation technique and reduction of the mesh size near the crack tip allow the crack path to be accurately predicted.

In the cylinders, the loading plates constrain the crack, so that it opens parallel to the plates. Thus, in compressed specimens the cracks are at angle to both the load direction and to the crack opening direction (§7). The cylindrical geometry is described by a combination of mode I and mode II crack propagation, with the same strain field on every longitudinal section.

The cylindrical symmetry of the cylinder allows the numerical computation to be simplified to a longitudinal section through the cylinder. In the longitudinal section of the cylinder in Fig. 17c, the two axes of symmetry are indicated. The presence of a second-order symmetry permits a further simplification, since only one-quarter of the longitudinal section need to be considered. The boundary conditions, loading direction, cracking direction and crack opening direction are shown in Fig. 14 (for a crack located in the bottom–left quarter of the longitudinal section in Fig. 17c). The 2nd-order symmetry of the section allows the boundary conditions for the whole of the bottom–left quarter to easily be computed: the displacements of the nodes lying on the axes of symmetry must be constrained according to a double pendulum.

In the compressive cylinder test model, the pre-cracking has been applied at the initiation point shown in Fig. 17c. The dimensions of the pre-crack have been fixed so as not to modify the stress field around the initiation point significantly.

The mixed-mode propagation tool proved to describe the propagation of the crack through the solid adequately. The crack path identified by the numerical model agrees with experimental observations (Figs. 21 and 22). By introducing material properties of the concrete into the numerical model for the cylinder test, the predicted average slope of the crack path agrees well with the one observed experimentally. It has a value of approximately 70° with respect to the horizontal direction.

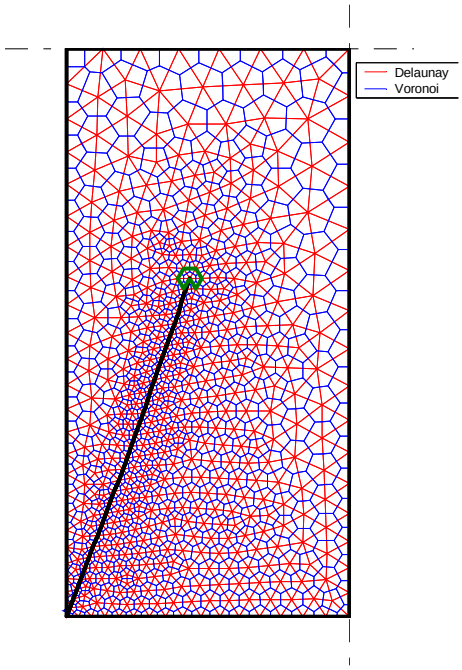

Figure 21: Numerically predicted crack path for a compressive cylinder test

Figure 22: Experimental crack path for a compressive cylinder test

Repeating the static analysis for various slenderness ratios, it was verified numerically [Ferretti (2001)] that the crack direction (for the same boundary conditions) is a property of the material and not of the solid geometry. This also agrees well with experimental experience.

As for the beam tests, the intra-element propagation technique and reduction of the mesh size near the crack tip allow the crack path to be accurately predicted.

9 Conclusions

A crack propagation analysis has been presented for use with the cell method, which combines nodal relaxation, intra-element propagation and remeshing. This method permits the mesh dimensions to be refined at specific locations, to improve the solution accuracy. The adopted mesh generator analyses multiple domains, and internal holes.

To describe crack propagation, the crack geometry is updated by introducing an extra node at the new crack tip. This is accompanied by a relaxation of the node at the old crack tip.

Both mode I, mode II, and mixed-mode crack propagation have been considered in this paper. The numerical model incorporates an original approach, which automatically estimates which part of the boundary is subjected to mode I loading, and which part is subjected to mode II loading. The numerical model subsequently estimates the size of the relative displacements between nodes on the opposite sides of the crack surface subjected to mode II loading, allowing sliding contact to be described.

The simulation is displacement-controlled.

All of the steps in the crack propagation process are completely automatic. When the crack tip is not stable:-

- the crack propagation direction is calculated;
- the crack geometry is updated;
- the mesh generator is invoked to revise the mesh;
- a static analysis and re-assessment of the crack geometry are repeated for the same value of displacement until the crack becomes stable.

During remeshing, the form of the mesh in the vicinity of the crack tip is pre-determined, leaving the mesh generator to generate the mesh in the remainder of the specimen.

Numerical and experimental results have been compared, showing that the numerical model is able to predict the evolution of cracks accurately.

Further studies are currently being undertaken to improve the efficiency of the numerical model.

The numerical results show that the CM numerical code can give good predictions for fracture mechanics problems, and validate the CM theory for fracture analysis.

An interesting development is associated with the crack propagation technique presented in this paper: by avoiding the discretization stage invoked by differential formulation, the CM requires less processing time than FEM codes. This aspect deserves additional, more thorough numerical analysis.

Furthermore, it is apparent that the CM, by using a direct finite formulation, avoids a problem associated with FEM codes: the stress around the crack tip does not approach infinity as the crack tip is approached. This represents the physical nature of the problem, since the $1/\sqrt{r}$ singularity at the crack tip is based on the hypothesis of an idealized elastic material [Muskhelishvili (1953), Westergaard (1939)].

It seems possible to identify a crack tip mesh size for which the numerical results are mesh independent. If this is indeed the case, accuracy problems at the crack tip are no longer a problem. This aspect of the analysis also deserves further work.

Acknowledgements Prof. Enzo Tonti is gratefully acknowledged for his suggestions and scientific supervision. This work was made possible by the Italian Ministry for Universities and Scientific and Technological Research (MURST).

References:

Atluri, S.N.; Shen, S. (2002): *The Meshless Local Petrov-Galerkin Method*, Tech Science Press.

Atluri, S.N.; Shen, S. (2002): The Meshless Local Petrov-Galerkin (MLPG) Method: A Simple \& Less-costly Alternative to the Finite Element and Boundary Element Methods. *CMES*, vol. 3, No. 1, pp. 11-52. Editor-in-Chief Atluri.

Atluri, S.N.; Zhu, T. (1998): A New Meshless Local Petrov-Galerkin (MLPG) Approach in Computational Mechanics. *Computational Mechanics*, vol. 22, pp. 117-127.

Barsoum, R. S. (1974): Application of Quadratic Isoparametric Finite Elements in Linear Fracture Mechanics. *Int J Fract*, vol. 10.

Barsoum, R. S. (1976): On the Use of Isoparametric Finite Elements in Linear Fracture Mechanics. *Int J Num Meth Engrg*, vol. 10, pp. 25-38.

Belytschko, T.; Lu, Y. Y.; Gu, L. (1994): Element Free Galerkin Methods. *Int J Num Meth Engrg*, vol. 37, pp. 229-256.

Benzeley, S. E. (1974) Representation of Singularities with Isoparametric Finite Elements. *Int J Num Meth Engrg*, vol. 8, pp. 537-545.

Benzeley, S. E.; Beisinger, Z. E. (1973): CHILES: A Finite Element Computer Program That Calculates the Intensities at Linear Elastic Singularities. *Sandia Laboratories Report*, SLA-73-0894.

Bouchard, P. O.; Bay, F.; Chastel, Y.; Tovena, I. (2000): Crack Propagation Modelling using an Advanced Remeshing Technique. *Comput Methods Appl Mech Engrg*, vol. 189, pp. 723-742. Elsevier

Carpinteri, A.; Sih, G. C. (1984): Damage Accumulation and crack Growth in Bilinear Materials with Softening: Application of Strain Energy Density Theory. *J Theor Appl Fract Mech*, vol. 1.2, pp. 145-160.

Cosmi, F. (2000): Applicazione del Metodo delle Celle con Approssimazione Quadratica. *Proc AIAS 2000*, pp. 131-140.

Di Tommaso, A. (1981): *Fondamenti di Scienza delle Costruzioni - Parte I*. Pàtron.

Erdogan, F.; Sih, G. C. (1963): On the Crack Extension in Plates under Plane Loading and Transverse Shear. *ASME J Basic Engrg*, vol. 85, pp. 519-527.

Fenner, R. T. (1996): *Finite Element Methods for Engineers*. Imperial College Press, London.

Ferretti, E. (2001): Rigenerazione Automatica della Mesh per la Modellazione della Propagazione del Crack nell'Ambito del Metodo delle Celle. *Proc AIMETA '01*, full text on CD-ROM.

Ferretti, E. (2001): *Modellazione del Comportamento del Solido Cilindrico Compresso*. Ph.D. Thesis, University of Lecce, Italy.

Ferretti, E.; Viola, E.; Di Leo, A. (2000): Impiego del Metodo delle Celle nella Stima dei Fattori di Intensificazione degli Sforzi. *Proc AIAS 2000*, pp. 699-708.

Ferretti, E.; Viola, E.; Di Leo, A.; Pascale, G. (1999): Propagazione della Frattura e Comportamento Macroscopico in Compressione del Calcestruzzo, *AIMETA '99*.

Ferziger, J. H.; Peric., M. (1997): Computational Methods for Fluid Dynamics. Springer.

George, P. L.; (1995): Automatic mesh generator using the Delaunay Voronoi principle. *Surv. Math. Ind.*, pp. 239-247.

Gurson, A. L. (1977): Continuum Theory of Ductile Rupture by Void Nucleation and Growth: Part I – Yield Criteria and Flow Rules for Porous Ductile Media. *J Engrg Mater Tech*, ASME, vol. 90, pp. 2-15.

Har, J. (1998): *A New Scalable Parallel Finite Element Approach for Contact-Impact Problems*. Ph.D. Thesis, Georgia Institute of Technology, Atlanta.

Harrop, L. P. (1985): The Optimum Size of Quarter-Point Crack Tip Element. *Int J Num Meth Engrg*, vol. 21, pp. 1911-1924.

Henshell, R. D.; Shaw, K. G. (1975): Crack Tip Elements Are Unnecessary. *Int J Num Meth Engrg*, vol. 9, pp. 495-509.

Huebner, K. H. (1975): *The Finite Element Method for Engineers*. Wiley.

Kim, H. G.; Atluri, S. N. (2000) Arbitrary Placements of Secondary Nodes, and Error Control, in the Meshless Local Petrov-Galerkin (MLPG) Method. *CMES*, vol. 1, No. 3, pp. 11-32. Editor-in-Chief Atluri.

Koenke, K.; Schmid, G. (1997): Prediction of Crack Propagation Directions under Plane Normal and Shear Loading. In: Meskouris, Wittek (eds), *Aspect in Modern Comp. Struct. Analysis*, pp. 431-441. Balkema Press, Rotterdam.

Livesley, R. K. (1983): *Finite Elements, an Introduction for Engineers*. Cambridge University Press.

Maiti, S. K.; Smith, R. A. (1984): Comparison of the Criteria for Mixed Mode Brittle Fracture Based on the Preinstability Stress-Strain Field – Part II: Pure Shear and Uniaxial Compressive Loading. *Int J Fract*, vol. 24, pp. 5-22.

Mavriplis, D. J. (1995): Multigrid Techniques for Unstructured Meshes. Von Karman Institute of Fluid Dynamics, Lecture Series 1995-02, *Computational Fluid Dynamics*.

Morton, K. W.; Stringer, S. M. (1995): Finite Volume Methods for Inviscid and Viscous Flows, Steady and Unsteady. Von Karman Institute of Fluid Dynamics,

Lecture Series 1995-02, *Computational Fluid Dynamics*.

Muskhelishvili, N. I. (1953): *Some Basic Problems on the Mathematical Theory of Elasticity*. Noordhoff-Groningen.

Nappi, A.; Rajgelj, S.; Zaccaria, D. (1997): Application of the Cell Method to the Elastic-Plastic Analysis. *Proc Plasticity '97*, pp. 14-18.

Nikishkov, G.P.; Park, J. H; Atluri, S.N. (2001): SGBEM-FEM Alternating Method for Analysing 3D Non-planar Cracks and Their Growth in Structural Components. *CMES*, vol.2, No.3, pp. 401-422. Editor-in-Chief Atluri.

Papadopoulos, P.; Jones, R. E.; Solberg J. (1995): A Novel Finite Element Formulation for Frictionless Contact Problems. *Int J Num Meth Engrg*, vol. 38, pp. 2603-2617.

Paris, P. C.; Erdogan, F. (1963): A Critical Analysis of Crack Propagation Laws. *ASME J Basic Engrg*, vol. 85, pp. 528-534.

Rashid, M. M. (1998): The Arbitrary Local Mesh Replacement Method: an Alternative to Remeshing for Crack Propagation Analysis. *Comput Methods Appl Mech Engrg*, vol. 154, pp. 133-150.

Rousselier, G. (1981): Finite Deformation Constitutive Relations Including Ductile Fracture Damage, *Three-Dimensional Constitutive Relations and Ductile Fracture*. In: S. Nemat-Nasser (ed), pp. 331-355.

Ruiz, G.; Ortiz, M.; Pandolfi, A. (2000): Three Dimensional finite-element simulation of the dynamic Brazilian Test on Concrete Cylinders. *Int J Num Meth Engrg*, vol. 48, pp. 963-994.

Sih, G. C. (1981): Analytical Aspects of Macro-Structure Mechanics, *Analytical and Experimental Fracture Mechanics*. (edited by Sih, G. C., and Mirabile, M.), Sijthoff and Noordhoff, pp. 3-15.

Sih, G. C. (1985): The Strain Energy Density Concept and Criterion, Special Issue in Fracture Mechanics Dedicated to G. R. Irwin and A. K. Rao. *J Aeronautical Soc India*, vol. 37, No. 1, pp. 43-60.

Sih, G. C.; DeLorenzi, H. G.; German, M. D. (1976): Crack Extension Modeling with Singular Quadratic Isoparametric Elements. *Int J Fract*, vol. 12, pp. 647-651.

Sih, G. C.; Liebowitz, H. (1968): Mathematical Theories of Brittle Fracture. *Fract*, vol. 2. Academic Press, New York.

Sih, G. C.; Macdonald, B. (1974): Fracture Mechanics Applied to Engineering Problems – Strain Energy Density Fracture Criterion. *Engrg. Fract. Mech.*, vol. 6, pp. 361-386.

Tonti, E., (2001): A Direct Discrete Formulation of Field Laws: the Cell Method. *CMES*, vol.2, No.2, pp. 237-258. Editor-in-Chief Atluri.

Westergaard, H. M. (1939): Bearing Pressures and Cracks. *J Appl Mech*, vol. 6, pp. 49-53.

Zhong, Z. H. (1993): Finite Element Procedures for Contact-Impact Problems. Oxford/New York/Tokyo, 372 pp., Book review: *Appl. Mech. Rev.*, vol. 48, No. 5, 1995, 5R4 (written by M Okrouhlik).

Zovatto, L. (2001): Nuovi Orizzonti per il Metodo delle Celle: Proposta per un Approccio Meshless. *Proc AIMETA '01*, full text on CD-ROM.